



Published in final edited form as:

IEEE Trans Med Imaging. 2010 February ; 29(2): 322–338. doi:10.1109/TMI.2009.2027993.

Image-Guided Intraoperative Cortical Deformation Recovery Using Game Theory: Application to Neocortical Epilepsy Surgery

Christine DeLorenzo [Student Member, IEEE],

Department of Biomedical Engineering, Yale University, New Haven, CT, 06520 USA

Xenophon Papademetris [Member, IEEE],

Departments of Biomedical Engineering and Diagnostic Radiology, Yale University, New Haven, CT, 06520 USA

Lawrence H. Staib [Senior Member, IEEE],

Departments of Electrical Engineering, Biomedical Engineering and Diagnostic Radiology, Yale University, New Haven, CT, 06520 USA

Kenneth P. Vives,

Department of Neurosurgery, Yale University School of Medicine, New Haven, CT, 06520 USA

Dennis D. Spencer, and

Department of Neurosurgery, Yale University School of Medicine, New Haven, CT, 06520 USA

James S. Duncan [Fellow, IEEE]

Departments of Electrical Engineering, Biomedical Engineering and Diagnostic Radiology, Yale University, New Haven, CT, 06520 USA

Abstract

During neurosurgery, nonrigid brain deformation prevents preoperatively-acquired images from accurately depicting the intraoperative brain. Stereo vision systems can be used to track intraoperative cortical surface deformation and update preoperative brain images in conjunction with a biomechanical model. However, these stereo systems are often plagued with calibration error, which can corrupt the deformation estimation. In order to decouple the effects of camera calibration from the surface deformation estimation, a framework that can solve for disparate and often competing variables is needed. Game theory, which was developed to handle decision making in this type of competitive environment, has been applied to various fields from economics to biology. In this paper, game theory is applied to cortical surface tracking during neocortical epilepsy surgery and used to infer information about the physical processes of brain surface deformation and image acquisition. The method is successfully applied to eight *in vivo* cases, resulting in an 81% decrease in mean surface displacement error. This includes a case in which some of the initial camera calibration parameters had errors of 70%. Additionally, the advantages of using a game theoretic approach in neocortical epilepsy surgery are clearly demonstrated in its robustness to initial conditions.

Keywords

Biomedical image processing; Image registration; Game theory; Brain; Surgery

I. Introduction

PRIOR to brain surgery, neurosurgeons may acquire images of different modalities to delineate pathologic regions requiring resection. One of the most challenging aspects during neurosurgery is the localization of these pathologic targets within the brain anatomy. The challenge is exacerbated when the pathologic structures, which are often visually indistinguishable from healthy tissue, lie within functionally eloquent areas [64]. Because of this, neurosurgeons have sought methods that allow visualization of underlying brain tissue or relay preoperative image information to the operating field [6], [31], [41], [48], [51]. Surgical navigation systems (SNS) aid target localization by providing neurosurgeons with preoperative brain images registered to the patient in the operating room (OR). Though these registrations are often performed with submillimeter accuracy [27], the alignment is rigid and therefore, movement of the soft tissue (brain shift) during surgery can cause a discrepancy between the displayed preoperative images and the current state of the brain, rendering the SNS unreliable from that point forward.

In addition to commercially-available SNS, some institutions have developed methods based on augmented reality to fuse intraoperative scenes with preoperatively-acquired images [14], [27], [45]. Such systems can match preoperative information with the operating field, as reconstructed from stereo images or captured by video. Even with these research systems, however, brain shift can prevent accurate visualization once the dura is opened [45].

Due to the complexity of the factors causing brain shift such as gravity, fluid loss and swelling [13], [23], [46], it is nearly impossible to predict the exact pattern of deformation preoperatively. Therefore, much research in this field has focused on acquiring intraoperative information to aid surgical guidance. Intraoperative volumetric images provide visualization of deformation throughout the entire brain; however, these methods suffer from potential drawbacks. For example, few groups consider using intraoperative computed tomography (iCT) for volumetric imaging, most likely due to the expense of the equipment, radiation exposure, necessary lead protection and poor soft tissue contrast [23], [28], [40], [57].

Since radiation exposure is not a problem with intraoperative ultrasound (iUS), an inexpensive modality in which volumetric images of the intraoperative brain are obtained by positioning a transducer on the exposed brain surface, some groups have focused on developing methods to register iUS images with preoperative magnetic resonance images (MRIs) [5], [7], [25], [34]. However, due to the different image characteristics (intensities, noise, contrast, field of view, dimensionality, etc.) of ultrasound and MRI, this type of intermodality registration can be challenging [46]. Because of this, Reinertsen *et al.* [46] avoided the intermodality registration and instead matched blood vessels from preoperative MR angiograms or gadolinium-enhanced MRIs with intraoperative blood vessels found by Doppler US. This method improved the registration implementation, although it required an extra (and possibly contrast-enhanced) set of images.

While the use of iUS is faster and less expensive, intraoperative magnetic resonance imaging (iMRI) has the added advantages of avoiding contact with the brain surface, producing high contrast images with better clarity and having imaging parameters that can be optimized depending on the image target [28], [40]. For this reason, information derived from iMRI is sometimes preferred [24], [28], [64]. Intraoperative MR implementation is either achieved using low-field MR scanners designed for the OR, which may result in suboptimal resolution [46], or adapting standard high field MRIs for OR use [42]. In either case, the cost of iMRI may be prohibitive for many hospitals. Additionally, each iMRI acquisition disrupts the surgery, lengthening total surgical time. This is not ideal because the

longer the patient is kept under anesthesia with the brain exposed, the higher the incidence of surgical complications, possibly from reactions to medications, bleeding or infection.

Since each volumetric imaging modality is either suboptimal or should be used sparingly, research has been performed on noninvasively tracking intraoperative cortical surface movement. If the cortical surface deformation is detected, this information can be used in conjunction with a biomechanical model to update preoperative brain images and reflect the intraoperative brain. Tracking of the cortical surface may not require volumetric imaging and can be accomplished with simple equipment such as a laser range scanner (LRS) or digital cameras. In addition, if intraoperative volumetric imaging is available, surface tracking can aid in the decision to perform volumetric imaging and can be used to monitor deformation between lengthier volumetric image acquisitions.

LRS measurements can be used directly to warp a preoperative image or indirectly as part of a deformation model [2], [10], [21], [40], [49], [50], [51]. The literature on LRS indicates that it has the potential to provide an alternative to the costly and restrictive modality of iMRI. It also has the advantages of not requiring brain surface contact, as with iUS, or the dose exposure of iCT. And, if LRS is used in conjunction with a digital camera, even more registration options are available [50]. However, the modality suffers from some resolution issues. It may be necessary to better calibrate the range data to achieve submillimeter accuracy. And, the subject of outliers, which tend to occur on the periphery of the images must be addressed [49].

Due to their portability and low cost, stereo camera imaging systems offer a viable option for intraoperative cortical surface detection [52], [53], [54], [56], [59]. The research on stereo vision, like that of LRS, indicates a promising non-invasive method of surface detection, which may also be subject to resolution errors. To characterize these errors, Sun *et al.* [57], [58] tested the accuracy of a rigid registration based on stereo-reconstructed features. Using a previously-constructed phantom [59], after a rigid transformation, the position of features extracted from CT images compared to those reconstructed from stereo imaging differed by up to 2.96 mm. These discrepancies (which often stem from inaccuracies in the stereo camera calibration) propagated through the nonrigid surface detection as well.

To obtain precise quantitative information from any imaging system, some type of calibration is usually necessary. In many real world situations, however, accurate camera calibrations are not possible [38]. This is especially true in the operating room, where extreme time and space constraints limit the calibration procedure possibilities. The resulting inaccurate camera calibrations compound the difficulty of image-derived deformation estimation. Consider Figure 1, which shows a single image of the intraoperative cortical surface. The imaged sulci are shown highlighted in black. Projected onto the images in green, by means of the camera calibration parameters (see Section II-D), are sulci extracted from the 3D intraoperative brain surface. To generate the left side of Figure 1, the 3D preoperative sulci were deformed to their correct intraoperative locations and then projected to image space, using inaccurate calibration parameters. The mismatch between these projected sulci and the outlined sulci is thus purely due to the effects of the camera calibration parameters. On the right side of Figure 1, the calibration parameters are correct, but the 3D preoperative (rather than intraoperative) sulci locations were projected to the image. This figure shows that the effects of calibration inaccuracies are not easily distinguishable from surface deformation. Therefore, in order to track a deforming cortical surface, a framework with the ability to solve for competing variables (surface displacement field and camera calibration parameters) is needed.

Game theory is the study of multiperson decision making [3]. It has historically been of great interest in fields such as business and economics in which decisions are made in a competitive environment [39]; however, it has been applied to disciplines ranging from philosophy to biology. Game theory has also made forays into the field of image analysis [9], [11], though, to our knowledge, its use has been restricted to image segmentation. In this work, a game theoretic framework is used to determine cortical surface displacement during neocortical epilepsy surgeries, based on intraoperative stereo image information.

Aside from the application of game theory to image registration, another considerable distinction between this and previous works is that the variables being updated (surface displacement/camera calibration parameters) are not explicitly contained in the images. That is, the images (preoperative MRI and intraoperative stereo camera images) are used to infer information about two physical processes (brain deformation/image acquisition), not image content. Thus, the contributions of this paper not only include extending the use of game theory to image registration, but also, the novel way in which game theory is applied to estimate deformation.

II. Method

The deformation estimation problem is modeled in a game theoretic formulation, in which the players are computational modules in a noncooperative game. In noncooperative games, collusion between players is prevented and the players pursue their own interests, which are partly conflicting with the others' [3]. Though the players of noncooperative games have competing objectives, the game may still reach an equilibrium state. In game theory, this state is referred to as the Nash equilibrium and it occurs when there is no incentive for any of the players to deviate from their current positions [11].

In this formulation of intraoperative neurosurgical guidance, the players are 1) \underline{U}_{dense} , the dense displacement field applied to the preoperative cortical surface, representing intraoperative deformation, and 2) $\underline{A} = [\underline{A}_0, \underline{A}_1]$, the camera calibration parameters from two views of the camera, which are used to transform points from the 3D intraoperative field into stereo image space (see Section II-D). Since changing the values of the camera calibration parameters can confound the search for the displacement field (see Figure 1), the most natural formulation of the intraoperative surface tracking problem is as a noncooperative game.

The game will terminate when the Nash equilibrium is reached, as this is the most rational compromise for each player. In this case, a particular instance of \underline{U}_{dense} , \underline{U}_{dense}^* , within the set of all possible dense displacement fields, \underline{U}_{dense}^* , and a particular instance of \underline{A} , \underline{A}^* , within the set of all possible calibration parameters, \underline{A}^* , is said to be at Nash equilibrium if [11]:

$$\begin{aligned} C_1 \left(\underline{U}_{dense}, \underline{A} \right) &\leq C_1 \left(\underline{U}_{dense}, \underline{A}^* \right), \quad \forall \underline{U}_{dense} \in \underline{U}_{dense}^* \\ C_2 \left(\underline{U}_{dense}, \underline{A} \right) &\leq C_2 \left(\underline{U}_{dense}, \underline{A} \right), \quad \forall \underline{A} \in \underline{A}^* \end{aligned} \quad (1)$$

where C_1 , C_2 are the cost functions corresponding to the decisions (values) for the dense displacement field and camera calibration parameters, respectively. These functions are described in more detail below.

It has been shown [11] that if the cost functions are of the form:

$$\begin{aligned} C_1(\underline{\mathbf{U}}_{dense}, \underline{\mathbf{A}}) &= F_1(\underline{\mathbf{U}}_{dense}) + \alpha F_2(\underline{\mathbf{U}}_{dense}, \underline{\mathbf{A}}) \\ C_2(\underline{\mathbf{U}}_{dense}, \underline{\mathbf{A}}) &= F_3(\underline{\mathbf{A}}) + \beta F_4(\underline{\mathbf{U}}_{dense}, \underline{\mathbf{A}}) \end{aligned} \quad (2)$$

and the constants, α and β , are chosen so that equation (3) is less than one:

$$\left\| \left[\left(\alpha^{-1} \frac{\partial^2}{\partial \underline{\mathbf{U}} \partial \underline{\mathbf{U}}} F_1(\underline{\mathbf{U}}) + \frac{\partial^2}{\partial \underline{\mathbf{U}} \partial \underline{\mathbf{U}}} F_2(\underline{\mathbf{U}}, \underline{\mathbf{A}}) \right)^{-1} \left(\frac{\partial^2}{\partial \underline{\mathbf{U}} \partial \underline{\mathbf{A}}} F_2(\underline{\mathbf{U}}, \underline{\mathbf{A}}) \right) \right] * \right. \\ \left. \left[\left(\beta^{-1} \frac{\partial^2}{\partial \underline{\mathbf{A}} \partial \underline{\mathbf{A}}} F_3(\underline{\mathbf{A}}) + \frac{\partial^2}{\partial \underline{\mathbf{A}} \partial \underline{\mathbf{A}}} F_4(\underline{\mathbf{U}}, \underline{\mathbf{A}}) \right)^{-1} \left(\frac{\partial^2}{\partial \underline{\mathbf{A}} \partial \underline{\mathbf{U}}} F_4(\underline{\mathbf{U}}, \underline{\mathbf{A}}) \right) \right] \right\| \quad (3)$$

then the Nash equilibrium exists. (The subscript for $\underline{\mathbf{U}}_{dense}$ was dropped in equation (3) for simplicity.)

Because equation (3) is an inequality, a range of values for α and β will satisfy this constraint. As long as the values of these constants are small, the constraints should be met, allowing the algorithm to converge. Though the range of acceptable values has been previously formally derived, it has also been shown that these values can be chosen empirically [11]. Preliminary tests revealed that when the algorithm converged, the results were not strongly sensitive to variations in α and β . Therefore, in this work, small values of α and β , which allowed successful convergence of the algorithm, were readily chosen empirically.

A Bayesian Approach to Surface Tracking

Cost functions for $\underline{\mathbf{U}}_{dense}$ and $\underline{\mathbf{A}}$ were designed using Bayesian analysis based on posterior probabilities given the information extracted from intraoperative stereo camera images and a preoperative MRI. (See Figure 2.)

$$\begin{aligned} C_1(\underline{\mathbf{U}}_{dense}, \underline{\mathbf{A}}) &= p(\underline{\mathbf{U}}_{dense} | \underline{\mathbf{I}}, \underline{\mathbf{K}}, \underline{\mathbf{C}}, S^U, \underline{\mathbf{A}}) \\ C_2(\underline{\mathbf{U}}_{dense}, \underline{\mathbf{A}}) &= p(\underline{\mathbf{A}} | \underline{\mathbf{I}}, \underline{\mathbf{K}}, \underline{\mathbf{C}}, S^U, \underline{\mathbf{U}}_{dense}) \end{aligned} \quad (4)$$

where $\underline{\mathbf{I}} = [I_0, I_1]$, the stereo camera images and $\underline{\mathbf{K}} = [K_0, K_1]$, the locations of the sulci in those images. Since the sulci can be detected in both the preoperative MRI and the stereo images, they are an important component of this analysis. At this point, the imaged sulci are manually extracted using an in-house graphical user interface and stored as 2D curves. This was easily implemented since the algorithm was tested off-line, post surgery. In the future, this extraction will be performed automatically. (See note below.) S^U is the undeformed preoperative brain surface, extracted from the MRI, and $\underline{\mathbf{C}}$ are the sulci on surface S^U . The 3D extraction of sulci is currently performed semiautomatically [18]. However, accurate sulcal segmentation has been accomplished by many groups using, for example, brain surface geometry, atlas-matching, or machine learning/neural networks [26], [35], [47], [60], [63], [66].

In words, equation (4) states that the model will determine the most likely surface displacement (from C_1) and camera calibration parameters (from C_2) given all the information obtainable from the preoperative MRI and the intraoperative stereo camera images.

A note on automatic sulci extraction from stereo images—Although an expert user can outline sulci of interest from a digital image in less than one minute, the application of any surface tracking algorithm is simpler when automated. Though automated sulci extraction does not fall within the scope of this work, there are several possibilities for decreasing the user input required for this step. If initial brain surface images are acquired at the beginning of surgery, the neurosurgeon (or other expert user) could easily outline the sulci of interest on these images using a graphical user interface. This would only have to be performed on the initial set of images. Segmentations of subsequent sulci could be performed automatically by nonlinearly warping the first set of images to the future corresponding stereo images, and thus determining the deformation of the sulci. The nonlinear warping of cortical surface images using an adaptive bases algorithm was extensively tested and has been successfully implemented by Sinha *et al.* [21], [49]. Besides nonlinear warping, sulci can also be tracked between images sets automatically using sophisticated contour/object tracking techniques from computer vision [12], [15], [16], [62]. In this case, if the initial camera calibration is accurate enough (as in the top row of Figure 6) the process can be completely automated, as the initial projections of the intraoperative sulci to the stereo image space can serve as shape priors for the contour matching. In order to automate this process without relying on the initial calibration, curve or edge-finding techniques can be used to extract the sulci. Such techniques are continually being developed and improved [4], [30], [33].

In a game theoretic framework, the objective is to minimize each player's cost function, which is the same as maximizing the negative of the cost function. Therefore, the expressions developed in this section can be written as maximizations, in which each objective function is maximized relative to one player while keeping the other fixed at each iteration.

Maximizing the expressions in equation (4) is equivalent to maximizing the log of the posterior probabilities:

$$\begin{aligned}\widehat{\mathbf{U}}_{dense} &= \underset{\mathbf{U}_{dense}}{\operatorname{argmax}} C_1(\mathbf{U}_{dense}, \widehat{\mathbf{A}}) \\ &= \underset{\mathbf{U}_{dense}}{\operatorname{argmax}} \log \left[p(\mathbf{U}_{dense} | \mathbf{I}, \mathbf{K}, \mathbf{C}, S^U, \widehat{\mathbf{A}}) \right]\end{aligned}\quad (5)$$

$$\begin{aligned}\widehat{\mathbf{A}} &= \underset{\mathbf{A}}{\operatorname{argmax}} C_2(\widehat{\mathbf{U}}_{dense}, \mathbf{A}) \\ &= \underset{\mathbf{A}}{\operatorname{argmax}} \log \left[p(\mathbf{A} | \mathbf{I}, \mathbf{K}, \mathbf{C}, S^U, \widehat{\mathbf{U}}_{dense}) \right]\end{aligned}\quad (6)$$

where $\widehat{\mathbf{U}}_{dense}$ and $\widehat{\mathbf{A}}$ are the updated values of the variables obtained at each iteration. For the first iteration, the value of $\widehat{\mathbf{U}}_{dense}$ is based on the distance between \mathbf{C} and the 3D reconstruction of \mathbf{K} (using the function Φ , defined in Appendix B-6) and the value of $\widehat{\mathbf{A}}$ is based on the initial camera calibration (Section II-D).

A. Displacement Field Optimization: Applying Bayes' Rule to equation (5) yields:

$$\begin{aligned}
\log \left[p \left(\mathbf{U}_{\text{dense}} | \mathbf{I}, \mathbf{K}, \mathbf{C}, S^U, \widehat{\mathbf{A}} \right) \right] &= \underbrace{\log \left[p \left(\mathbf{I}, \mathbf{K}, \mathbf{C}, S^U, \widehat{\mathbf{A}} | \mathbf{U}_{\text{dense}} \right) \right]}_{\text{Displacement Term}} \\
&+ \underbrace{\log \left[p \left(\mathbf{U}_{\text{dense}} \right) \right]}_{\text{Prior Term}} - \underbrace{\log \left[p \left(\mathbf{I}, \mathbf{K}, \mathbf{C}, S^U, \widehat{\mathbf{A}} \right) \right]}_{\text{Constants}}
\end{aligned} \quad (7)$$

The Displacement Term may be rewritten as:

$$\begin{aligned}
\log \left[p \left(\mathbf{I}, \mathbf{K}, \mathbf{C}, S^U, \widehat{\mathbf{A}} | \mathbf{U}_{\text{dense}} \right) \right] &= \log \left[p \left(\widehat{\mathbf{A}} | \mathbf{U}_{\text{dense}} \right) \right] \\
&+ \log \left[p \left(\mathbf{I}, \mathbf{K}, \mathbf{C}, S^U | \widehat{\mathbf{A}}, \mathbf{U}_{\text{dense}} \right) \right]
\end{aligned} \quad (8)$$

Assuming the independence of the sulci from the surface and images, equation (8) can be further developed.

$$\begin{aligned}
\log \left[p \left(\mathbf{I}, \mathbf{K}, \mathbf{C}, S^U, \widehat{\mathbf{A}} | \mathbf{U}_{\text{dense}} \right) \right] &= \underbrace{\log \left[p \left(\widehat{\mathbf{A}} | \mathbf{U}_{\text{dense}} \right) \right]}_{\log \left[p \left(\widehat{\mathbf{A}} | \mathbf{U}_{\text{dense}} \right) \right]} \\
&+ \underbrace{\log \left[p \left(\mathbf{I}, S^U, \widehat{\mathbf{A}} | \mathbf{U}_{\text{dense}} \right) \right] - \log \left[p \left(\widehat{\mathbf{A}} | \mathbf{U}_{\text{dense}} \right) \right]}_{\log \left[p \left(\mathbf{I}, S^U | \widehat{\mathbf{A}}, \mathbf{U}_{\text{dense}} \right) \right]} \\
&+ \underbrace{\log \left[p \left(\mathbf{K}, \mathbf{C}, \widehat{\mathbf{A}} | \mathbf{U}_{\text{dense}} \right) \right] - \log \left[p \left(\widehat{\mathbf{A}} | \mathbf{U}_{\text{dense}} \right) \right]}_{\log \left[p \left(\mathbf{K}, \mathbf{C} | \widehat{\mathbf{A}}, \mathbf{U}_{\text{dense}} \right) \right]}
\end{aligned} \quad (9)$$

Combining equations (7)-(9) yields:

$$\begin{aligned}
\log \left[p \left(\mathbf{U}_{\text{dense}} | \mathbf{I}, \mathbf{K}, \mathbf{C}, S^U, \widehat{\mathbf{A}} \right) \right] &= \underbrace{\log \left[p \left(\mathbf{I}, S^U, \widehat{\mathbf{A}} | \mathbf{U}_{\text{dense}} \right) \right]}_{\text{Intensity Term}} \\
&+ \underbrace{\log \left[p \left(\mathbf{K}, \mathbf{C}, \widehat{\mathbf{A}} | \mathbf{U}_{\text{dense}} \right) \right]}_{\text{Feature Term}} + \underbrace{\log \left[p \left(\mathbf{U}_{\text{dense}} \right) \right]}_{\text{Prior Term}} \\
&- \underbrace{\log \left[p \left(\mathbf{I}, \mathbf{K}, \mathbf{C}, S^U, \widehat{\mathbf{A}} \right) \right] - \log \left[p \left(\widehat{\mathbf{A}} | \mathbf{U}_{\text{dense}} \right) \right]}_{\text{Constants}}
\end{aligned} \quad (10)$$

The terms of equation (10) are developed in Appendix A.

B. Camera Calibration Calculation: The expansion of the camera calibration term can proceed in the same fashion as the dense displacement field. Applying Bayes' Rule to equation (6) yields

$$\begin{aligned} \log \left[p \left(\underline{\mathbf{A}}, \underline{\mathbf{I}}, \underline{\mathbf{K}}, \underline{\mathbf{C}}, S^U, \widehat{\mathbf{U}}_{\text{dense}} \right) \right] &= \underbrace{\log \left[p \left(\underline{\mathbf{I}}, \underline{\mathbf{K}}, \underline{\mathbf{C}}, S^U, \widehat{\mathbf{U}}_{\text{dense}} | \underline{\mathbf{A}} \right) \right]}_{\text{Calibration Term}} \\ &+ \underbrace{\log \left[p \left(\underline{\mathbf{A}} \right) \right]}_{\text{Prior Term}} - \underbrace{\log \left[p \left(\underline{\mathbf{I}}, \underline{\mathbf{K}}, \underline{\mathbf{C}}, S^U, \widehat{\mathbf{U}}_{\text{dense}} \right) \right]}_{\text{Constants}} \end{aligned} \quad (11)$$

The terms of equation (11) are developed in Appendix B.

C. Model Reformulation: Using the Bayesian analysis outlined in Appendices A and B (equations 22 and 26), the model for determining cortical surface displacement and camera calibration can be expressed in same form as equation (2):

$$\begin{aligned} \mathbf{C}_1 &= \underbrace{T_U \left(\underline{\mathbf{U}}_{\text{dense}} \right)}_{\text{smoothness constraint}} + \alpha \left[\underbrace{T_F \left(\underline{\mathbf{U}}_{\text{dense}}, \underline{\mathbf{A}} \right)}_{\text{feature matching}} + \underbrace{T_I \left(\underline{\mathbf{U}}_{\text{dense}}, \underline{\mathbf{A}} \right)}_{\text{intensity correlation}} \right] \\ \mathbf{C}_2 &= \underbrace{T_A \left(\underline{\mathbf{A}} \right)}_{\text{fiducial matching}} + \beta \left[\underbrace{T_C \left(\underline{\mathbf{U}}_{\text{dense}}, \underline{\mathbf{A}} \right)}_{\text{reconstructed sulci matching}} \right] \end{aligned} \quad (12)$$

where T_U is a prior on the deformation field, T_F and T_I match the features and intensities, respectively, of the deformed cortical surface to the intraoperative stereo images, T_A is a prior on the camera calibration and T_C matches the stereo-reconstructed sulci to the deformed cortical sulci.

D. Camera Calibration Parameters: For simplicity, the camera calibration parameters were initially represented as matrices [17], [20]. However, since a simple projection matrix cannot entirely capture the image acquisition process, these matrices are not physically meaningful. Even the rotation component of the transformation matrix is an approximation [61]. While this may be suitable for many stereo applications, tracking intraoperative brain shift requires extremely high accuracy. To account for this, a new model was developed which includes parameters for rotation, translation, focal length, principal point, lens distortion and skew, based on the internal camera model by Heikkilä [29]. Using these calibration parameters, the projection of any 3D point to an image can easily be calculated with standard stereo vision methods [29] or even from commercial software packages [8]. This projection process, adapted from [8], is outlined below.

First, a 3D point in the camera reference frame, (X_c, Y_c, Z_c) , is projected to an image using a pinhole camera projection model, where $x_n(1) = X_c/Z_c$ and $x_n(2) = Y_c/Z_c$. In this case, \mathbf{x}_n is the normalized pinhole projection. Next, point coordinates which account for lens distortion are calculated, \mathbf{x}_d . This formulation models lens distortion using sixth order polynomial terms as a function of the distance from the optical axis. These coordinates, \mathbf{x}_d , are equal to $(1 + k_c(1)r^2 + k_c(2)r^4 + k_c(5)r^6)x_n + \mathbf{dx}$, where $r^2 = x_n(1)^2 + x_n(2)^2$ and \mathbf{k}_c is the 5×1 vector of image distortion coefficients. The tangential distortion vector, \mathbf{dx} , is equal to $[2k_c(3)x_n(1)x_n(2) + k_c(4)(r^2 + 2x_n(1)^2)k_c(3)(r + 2x_n(2)^2) + 2k_c(4)x_n(1)x_n(2)]^T$. Once the distortion is applied, the final pixel coordinates can be found by setting $[x \ y \ 1]^T$ equal to $K_{\text{camera}} * [x_d(1) \ x_d(2) \ 1]^T$, where K_{camera} is referred to as the camera matrix and is defined

as $[f_x \alpha_c f_x o_x; 0 f_y o_y; 0 0 1]$. In this matrix, (f_x, f_y) is the focal length in pixels, (o_x, o_y) is the principal point and α_c is the skew coefficient.

Once determined, calibration parameters are used to transform points from registered patient space (preoperative MRI space - see Section II-E) to stereo image space. These parameters will more reliably perform the projections and backprojections required for the game theoretic algorithm than a simplified projection matrix. (Backprojection is a method of assigning intensity values from an image to a surface. See Appendix A.) It is possible to calculate the expanded model parameters directly from images of a calibration pattern in different poses [8]. This could be accomplished in the OR, for example, by locating the corners of the calibration object in each position using a tracking tool. Unfortunately, this unwieldy and time consuming calibration process is often not feasible in the OR due to time constraints. There is usually only enough time to calibrate the system using one tracked pose of the calibration pattern.

Since the calibration parameters will be updated at every iteration (equation (6)), though, only a rough estimate of these parameters is needed to initialize the algorithm. Most of these parameter estimates can be extracted from the projection matrices obtained from a standard calibration procedure using one tracked pose [61]. (See Section II-E for the calibration procedure.) Any parameters not directly estimated from those projection matrices can be initialized to zero and determined by the algorithm. In this way, using a game theoretic approach provides all of the advantages of an expanded calibration model without the necessity of an expanded calibration technique.

E. OR Protocol: Two transformations are needed in order to warp the preoperative brain image to the deformed intraoperative brain. The first is a rigid transformation between the preoperative MRI, acquired on a Siemens 1.5 Tesla Sonata system (Siemens AG, Munich, Germany), and the patient in the OR. The second is the nonrigid transformation calculated using the game theoretic algorithm.

1) Rigid Registration: This transformation is calculated immediately before surgery begins, as part of the standard procedure required for SNS use. It is performed by locating facial landmarks on the patient, either manually or using a laser striping technique. These landmarks are then matched to the patient's preoperative images and the rigid transformation relating the two point sets is calculated. In this work, a BrainLAB Surgical Navigation Station (BrainLAB AG, Feldkirchen, Germany) with BrainLAB's VectorVision (VV) navigation software was used for rigid patient registration [43].

Once the rigid registration is performed, markers can be placed on surgical tools, allowing them to be detected by BrainLAB infrared cameras and displayed on a monitor relative to the patient's preoperative MRI. In the same way, a pointer tool can be used to touch any location visible to the infrared cameras and the 3D coordinates of the pointer tip will be transformed into the space of the preoperative image (using the calculated rigid transformation matrix) and recorded. Recorded 3D locations can be exported to any computer by connecting to the BrainLAB SNS through the VV Link interface [43] using the Yale BioImage Suite software package [44].

2) Nonrigid Registration: This is the transformation computed by the game theoretic algorithm, requiring the following intraoperative information: the brain surface intensities from two camera positions (stereo camera images), the locations of fiducial markers in each camera position, and the corresponding 3D locations of the imaged fiducial markers. (See Figure 2.) Obtaining this information was the only change to the surgical work flow normally implemented for these surgeries.

Fiducial markers are used to calculate the initial camera calibration parameters and to guide the calibration optimization routine. Any calibration target (sterile object with discrete identifiable features and known dimensions) can be used for this procedure; however, in this work, a sterile grid of electrodes was used. Since the electrodes are numbered, they are easily found by the neurosurgeon using the BrainLAB pointer tool and distinguished in the stereo camera images. These types of electrodes may be used for epilepsy monitoring and are sometimes placed around suspected epileptogenic regions to record the origin and spread of electrical signals associated with the patient's seizures. However, most of the electrode grids used in this work were unrelated to the surgery and specifically used for the calibration procedure. The grids were placed on the brain surface during the image acquisitions and then removed, not implanted for patient monitoring. In this way, it is possible to use these grids for calibration during surgical procedures other than electrode implantation.

A single camera embedded in one of the OR light fixtures (standard OR equipment for documenting surgeries) was used for cortical surface imaging. Each fixture has an attached handle, allowing the surgeon (or OR staff) to quickly move the light and camera into an appropriate position. The camera's view was displayed on a monitor in real time, providing a preview of each image before it is saved. If necessary, the camera could also be rotated and its zoom factor changed remotely.

Although two cameras are often used for stereo imaging, positioning a fixed stereo camera system within the crowded (with people and equipment) and busy OR is difficult. The advantages of using a single camera set up are: (1) a single camera can be easily positioned by the neurosurgeon to obtain an unobstructed view of the surgical field (Figure 3 Left) no matter which direction the patient is oriented and (2) this setup does not increase the amount of OR equipment needed.

To acquire stereo images, the calibration/imaging procedure outlined on right side of Figure 3 was used. Note that the camera is calibrated each time it is repositioned. An alternative to this procedure would be to calibrate the camera once and then track its position in 3D space, as in [57]. However, since the entire repositioning/recalibration procedure took less than five minutes to complete and did not require the purchase of additional equipment, it is a feasible option.

The surface tracking technique was performed during electrode implantations or ictal tissue resections associated with neocortical epilepsy, as summarized in Table I.

III. Results

A. In Vivo Surface Tracking with Game Theory

Game theoretic cortical surface tracking was used in five separate surgeries for a total of eight data sets. Two of these data sets were from a bilateral craniotomy performed on one patient. (Data set #2 was obtained from the left dural opening and data set #3 from the right. See Table I.) Since the surgeries were performed simultaneously, the patient had to be oriented so that both hemispheres were accessible. Because of this, the direction of gravity was parallel to the plane of the dural openings rather than perpendicular to them, as is normally the case, providing two excellent test cases for the robustness of the algorithm.

The algorithm results for all cases are shown in Figure 4. Since the positions and sizes of the craniotomies varied as well as the time into surgery in which the algorithm was applied (Table I), the amount of cortical deformation also varied. Therefore, on the left side of Figure 4, the calculated mean average displacement of the cortical surface as predicted by the game theoretic algorithm is shown for reference (blue bars). Mean residual error of the

algorithm (red bars) is calculated by averaging the closest distances between the predicted surface and sparse (between five and twenty-one, depending on dural opening size) cortical surface points touched with a 3D locator intraoperatively. Five out of eight of the cases (62.5%) resulted in a mean algorithm error of less than 1.0 mm, and the mean error never exceeded 1.70 mm. These results indicate accurate cortical tracking and an 81% improvement over uncompensated error.

While the mean errors were quite low, it is also important to examine the maximum error of the algorithm in each case. The right side of Figure 4 indicates the decrease in maximum error using the game theoretic algorithm. For half the cases, the maximum error was under 1.6 mm, despite surface displacements greater than 14 mm. And, overall, there was a 76% decrease in the maximum errors using model guidance. This finding is very important because it indicates that the algorithm not only decreases the mean error, but it never increases the maximum surface error. Thus, for all eight cases, the cortical surface was more accurately located with the tracking algorithm than by relying on the preoperative surface views as derived from the MRI.

B. In Vivo Sample Cases

The results of the *in vivo* studies in aggregate were very encouraging, revealing that the algorithm provided surface tracking advantages in all eight cases. In order to further examine the usefulness of the calibration correction and displacement tracking, a representative sample of the *in vivo* cases is described in detail below.

1) Data Sets 4 and 5—Data sets 4 and 5 are interesting because they were acquired from two time points of the same surgery. Stereo images for data set #4 were taken approximately two hours into surgery and the images for data set #5 were taken seventy-five minutes later. Since no surgical manipulations were performed in that period, the deformation observed during that time was the result of gravity. The calculated deformations from these two data sets were consistent not only with surface points used for validation, but also, with each other, though they were computed independently. (See Figure 5.)

The mean surface deformation of data set #4 was 4.48 mm. The accuracy in tracking this deformation is shown both quantitatively, in Figure 4, which reveals the mean surface error was reduced to under 1 mm, and qualitatively in Figure 6, which shows the agreement of intensity and feature positions using algorithm results. The top left row of Figure 6 shows that, initially, sulci projected from the preoperative brain surface (green) were not aligned with features extracted from the stereo images (black), due to a combination of intraoperative brain shift and possible camera calibration errors. Using the game theoretic surface tracking algorithm, updated camera calibration parameters and a cortical surface displacement field were calculated. The displacement field was then applied to the preoperative brain surface and the deformed positions of the sulci were projected to the stereo images using the updated camera parameters. As shown in the bottom row of Figure 6, using the calculated deformation and calibration, the features are better aligned.

The intensities are also better matched, as can be seen on the right side of Figure 6. The intensities that are backprojected from camera position 0 better match the intensities backprojected from camera position 1 when the surface is in its predicted location and the updated calibration parameters are used. Additionally, the updated deformation and camera parameters better align the backprojected sulci with the sulci extracted from the surface.

However, the more interesting case is data set #5 because the initial calibration performed in camera position 1 was so poor that the projected features were not contained within the image. This can easily occur when the procedure is rushed, resulting in either few fiducial

locations to guide the calibration or errors in locating the centers of the fiducial markers (the L_i in equation (25)). Though a more accurate initial calibration could have been performed by using a more extensive calibration procedure, there was not enough time to perform this type of lengthy procedure in the OR.

Because of the calibration inaccuracies, the right stereo camera image of Figure 7 shows two highly distorted green lines instead of the expected curved sulci. The effect is also seen in the backprojected images of Figure 7, in which the top right surface is mostly out of the view of the camera and therefore is not assigned intensity values. In order to correct these errors, the calibration parameters needed to be drastically changed. (See Table II.)

Even in the presence of both this large calibration error and a greater surface deformation (6.59 mm mean displacement), the algorithm was able to correct the camera calibration distortion and align the cortical features, reducing the mean surface error to 0.39 mm. The bottom row of Figure 7 shows the positions of the projected sulci using the updated displacement field and calibration parameters (yellow). These features are much better aligned with their intraoperatively imaged counterparts (black). Additionally, the predicted surface location (bottom right surface of Figure 7) is not only in the camera view, but also, its backprojected intensities are aligned with the surface features. There is some residual distortion on the lower part of the right backprojected image (bottom right of Figure 7), outside of the calibration region; however, it is minimal.

2) Data Set #8—Aside from examining the cases in which the game theoretic algorithm performs well, it is also important to understand when it performs suboptimally. The initial camera calibration of data set #5 produced inaccurate values of the calibration parameters. However, these parameters were corrected with equations (24) and (25). In the case of data set #8, it is likely that the camera calibration failed for a different reason, leading to a mean residual error of greater than 1.5 mm. (See Figure 8.)

In this surgery, the shape of the cortical surface made it difficult to position the electrode grid used for the initial calibration. (See Figure 9.) Because the grid did not sit well on the brain, it is possible that the grid was moved each time it was touched for fiducial locations. Since the error was due to the offset of the grid and not random localization error, the assumption of Gaussian error in the prior term may not have been valid in this case. (See Appendix B-7.) However, overall, the mean surface error was still improved using the game theoretic result, as seen in Figure 4. This is most likely because the reconstructed sulci matching term of equation (12) also updated the camera calibration parameters and was able to correct some of the error.

C. Algorithm Robustness Comparison

In order to further examine the advantages of using a game theoretic framework, it was compared to three other surface tracking algorithms: (1) A single objective function in which, at each iteration, the camera calibration parameters and the dense displacement field are optimized together. The single objective function, $SO(\mathbf{U}_{dense}, \mathbf{A}) = T_U(\mathbf{U}_{dense}) + \alpha [T_F(\mathbf{U}_{dense}, \mathbf{A}) + T_A(\mathbf{U}_{dense}, \mathbf{A})] + T_A(\mathbf{U}_{dense}) + \beta T_C(\mathbf{U}_{dense}, \mathbf{A})$, is comprised of all the unique terms in the objective functions C_1 and C_2 (equation 12). It is therefore based on the same Bayesian analysis used to develop the game theoretic algorithm; however, the dense displacement field and camera calibration optimization are performed in a single step. (2) The cost function, C_1 , solved without calibration compensation. Although the expression for C_1 contains calibration dependent terms, the optimization is only performed over the dense displacement field, using the initial calibration. And, (3) an iterative scheme in which the single objective function, $SO(\mathbf{U}_{dense}, \mathbf{A})$, is iteratively updated over \mathbf{U}_{dense} and \mathbf{A} . This

method was the original framework developed to account for camera calibration inaccuracies [20]. Optimization by gradient descent was used in all three cases.

The use of (1) and (3) allow one to determine the advantages, if any, of using a game theoretic framework to solve the tracking problem as a noncooperative game. This comparison will show whether the Nash equilibrium is a better solution than the minimum of a single objective function, updated over \mathbf{U}_{dense} and \mathbf{A} either jointly or iteratively. The comparison to (2) will show whether calibration compensation improves or degrades a displacement-only deformation estimation. To make this a fair comparison, a data set was chosen in which the initial calibration yielded accurate results even without calibration correction.

Figure 10 shows the robustness of each algorithm to initialization for an *in vivo* case (data set #2 in Figure 4). The plot on the left was generated by adding a range of offsets to the initial surface position. The single objective function, both solved jointly (red) and iteratively (green), is more sensitive to the offsets because it cannot resolve whether the initial error is a result of calibration error or deformation. Using a single objective function, the camera calibration parameters could be distorted so much that they will minimize the cost, even with an incorrect displacement field, or vice versa. Accurate tracking could only be performed when the camera calibration parameters were forced to stay fixed (black) or when game theory was used to distinguish between the two types of errors (blue).

As expected, the main difference between using a game theoretic approach and a pure displacement algorithm is revealed in the presence of camera calibration error. The right side of Figure 10 was generated by offsetting the translation component of the calibration parameters by increasing percentages. This offset prevents 3D points from being accurately transformed into the camera coordinate system, and they will therefore be improperly projected into image space. (In other words, the (X_c, Y_c, Z_c) coordinates of Section II-D will be offset.) The cortical intensities from the stereo images will also be improperly backprojected onto the 3D surface. Without proper compensation for the calibration parameters (black), the mean algorithm error increases dramatically as calibration error increases. As before, a single objective function (red/green) cannot resolve the source of the error, regardless of the way in which it was optimized (jointly/iteratively). The mean error of all algorithms, with the exception of the game theoretic approach, rises above 4 mm once the calibration error reaches 5%. Even at 15% calibration error, it is better to use the game theoretic framework than to rely on the uncompensated preoperative surface for surgical guidance.

IV. Summary and Conclusions

The game theoretic algorithm developed in this paper was proven to be robust in both simulations and *in vivo* neocortical epilepsy surgeries. However, there are some limitations to the system that will need to be addressed.

A. System Limitations and Future Work

1) Volumetric Results—The game theoretic algorithm only provides deformation estimates at, or near, the brain surface. Though no method can predict deformation completely, biomechanical models can produce deformation estimates within the brain volume. Sophisticated models have been developed for this purpose and one such model has already been used in conjunction with game theoretic surface tracking [18]. When used in this way, deformation accuracy within the brain volume is a combination of the game theoretic and volumetric model accuracy. Though this accuracy may worsen for structures

lying deeper within the brain, the combination of surface and volume based deformation estimation may be one method of providing surgical navigation to the entire brain.

In surgeries in which large amounts of tissue are removed, such as temporal lobectomies or tumor resections, a biomechanical model based on the preoperative brain would no longer be valid. In this case, some type of intraoperative volumetric imaging would be necessary. To avoid the long acquisition times of multiple intraoperative volume scans, a system could be developed in which game theory is used to update the preoperative images and guide the surgery until tissue is removed. At that point, a volume image from iMRI/iCT/iUS could be acquired to establish the updated brain volume. A new mesh of the brain could then be created and process can resume with the updated brain mesh. This type of application would most likely also require a more detailed biomechanical model. Such models are currently in development [1], [13], [22], [23], [32], [36], [37], [55], [65] and, as shown in [18], could easily be applied in conjunction with the game theoretic surface detection. These solution possibilities can be tested in phantom experiments or on *ex vivo* tissue.

2) Surface Visibility—As with any system that tracks a visible surface, stereo vision is dependent on surface visibility. Therefore, if the brain surface is significantly disrupted during surgery (due to, for example, bleeding or tissue resection), it may be difficult to determine the locations of the sulci. The algorithm would then have to rely mostly or entirely on the matching of intensities, which could lead to inaccuracies. In the worst case, surface disruptions can significantly change the surface intensities, violating the image similarity assumption in the intensity term of equation (10), possibly preventing the effectiveness of this term. If these effects are due to bleeding, neurosurgeons would need to irrigate the area, to clear as much blood as possible before acquiring the stereo images. If the effects are due to tissue resection or they cannot be cleared, it may still be possible to use this algorithm; however, instead of using stereo cameras to detect the sulci, sulcal positions would have to be manually located using the 3D pointer tool. In this way, stereo reconstruction would not be needed since 3D sulcal locations would be used as inputs. Still, this will only be valid if most of the surface geometry were preserved. Effects of tissue resection remain an open problem for most surgical guidance systems.

3) Algorithm Optimization—Although this study showed that results based on a game theoretic approach are highly accurate *in vivo*, further optimization of the algorithm could lead to higher accuracy or aid in situations similar to that explained above in which one term of the model becomes unreliable. In this work, weighting constants for feature, intensity and prior terms were chosen empirically and fixed for all cases. It may be more advantageous, however, to adapt the weighting constants to each case. For example, if the intensities in one set of intraoperative images were fairly constant, those intensities may not aid the surface tracking. In this case, a better result could be obtained by decreasing the intensity term weight or increasing the weight assigned to the feature term. As another example, the smoothness constraint could be weighted less if tissue resection causes the surface to become jagged.

In order to determine how to vary the weights, a systematic approach for measuring the quality of each variable must be developed. This could be accomplished by assessing each parameter's attributes. For example, to determine the reliability of the intensity term, image histograms can be evaluated. For the feature term, weights could be determined based on the number of features present and their coverage of the exposed surgical field. Similarly, assessing the sources of initial calibration error and basing the prior distribution on this assessment could improve the algorithm solution accuracy in cases like data set #8.

4) Algorithm Validation—To save time in the operating room, fiducial points on the brain surface were used both as part of the camera calibration and as validation points to calculate algorithm accuracy. There is no reason to believe that this would bias the results since, as mentioned, the final calibration parameters are not based exclusively on fiducial locations but instead result from the iterative game theoretic optimization. A leave-one-out strategy was employed to test this assumption for two cases (data sets 4 and 5 from Section III-B). The game theoretic algorithm applied to each combination of N-1 fiducial markers (where N is the total number of fiducial markers) to update the calibration parameters, and the residual algorithm error was calculated from the marker that was excluded from use. The mean algorithm error using this leave-one-out strategy was 0.52 mm for data set #4 (maximum = 1.52 mm) and 0.46 mm for data set #5 (maximum = 0.78 mm). Using a paired t-test to compare the residual algorithm error at each fiducial marker when it was excluded versus included in the game theoretic algorithm analysis revealed no statistical differences, at a 5% significance level, for both data sets (data set 4: p-value = 0.11, 95% CI = -0.18:0.02; case 5: p-value = 0.53, 95% CI = -0.17:0.31). Though this helps to confirm the assumption that using fiducial markers as validation points does not affect the algorithm result, further testing will be performed in the future.

5) Fiducial Marker Localization—Lastly, manual location of fiducial markers can also be a source of error. Though SNS can achieve submillimeter accuracy [27], this accuracy is only measured between the actual location of the 3D pointer and the detected location of the 3D pointer; it does not account for the user's repeatability in touching the desired target with the pointer. To independently measure this, an expert user was asked to touch four electrodes on the grid three times each. To create a realistic recreation of what occurs in the OR, the electrode grid was placed on top of a silicone brain phantom [19] so that, depending on the amount of force applied, the pointer could depress the electrode along with the surface underneath that electrode (as could happen in the OR with the brain surface). The localization error was calculated as the distance between each of the three trials and mean location (of the three trials). The mean localization error for all four electrodes was 1.19 mm (standard deviation: 0.50 mm; range: 0.33 mm - 3.10 mm). This indicates that, in some cases, the points used for validation may be inaccurately located. However, on average, fiducial localization is within 1.2 mm of the target. In future studies, calibration targets will be designed to minimize fiducial localization error, for example, by being more rigid.

B. Conclusions

The results outlined in Section III-A indicate that the developed game theoretic algorithm can accurately track a deforming surface *in vivo*. Figure 4, showing the algorithm results for all eight intraoperative neocortical epilepsy cases, reveals the algorithm's tracking potential over a range of cases. Large deformations (up to 14 mm) and varying patient orientations, including one patient with bilateral craniotomies (data sets 2 and 3) did not affect the algorithm error, which never rose above 1.7 mm.

The illustrations from data sets 4 and 5, which provide visual validation of the algorithm solution, show that the game theoretic result aligns both the feature and intensity information from the stereo camera images. The results are consistent with validation points acquired by the neurosurgeon and make intuitive sense relative to each other. Data set #5 is particularly interesting due to its initial large amount of calibration error, which the algorithm is able to correct. Examination of data set #8 shows a similar effect, in that the feature and intensity matching is improved using the updated calibration parameters and displacement field. However, this case shows the reliance of the algorithm on the distribution of the initial calibration error. Regardless of this reliance, using the tracking algorithm in this case, as in all of the cases tested, still produced an advantage over relying

solely on preoperative images. These results are very encouraging and indicate the potential of a surface tracking algorithm posed with game theory to improve surgical navigation.

The robustness comparison shows that, in the absence of calibration error, the algorithm based on game theory performs at least as well as a pure displacement cost function and that the addition of the camera calibration optimization did not decrease the surface tracking accuracy. With the other paradigms tested, camera calibration optimization interfered with displacement field detection and led to a suboptimal result. This does not mean that it is impossible to achieve accurate results in these paradigms. However, it does reveal the problems that may arise from solving for competing variables in a single objective framework.

The robustness comparison also clearly shows the deleterious effects that camera calibration error can have on the ability to track a moving surface. Since most algorithm terms rely on the calibration parameters in some way, and because calibration errors are difficult to distinguish from surface deformation effects (see Figure 1), it is no surprise that calibration error can propagate through the algorithm solution. The algorithm based on game theory outperforms all the other methods tested in this context, thus proving its ability to separate calibration and deformation effects and demonstrating its robustness to a range of initial calibration inaccuracies.

Future work on this algorithm could further enhance its accuracy by allowing dynamic choices of the weighting terms based on assessments of the algorithm inputs. In addition, the application of this algorithm can be expanded beyond procedures relating to epilepsy. Although particularly useful in neocortical epilepsy surgeries due to the great need for surface deformation information during epilepsy monitoring and tissue resection, this intraoperative deformation compensation algorithm could be applied to many neurosurgical procedures (since dural openings ≈ 4 cm in diameter, which normally occur when the patient undergoes a craniotomy, will allow for adequate intensity/feature detection). And, when used in conjunction with a biomechanical model and/or volumetric imaging, the range of neurosurgical procedures that would benefit from this tracking technique becomes even larger; although, surgeries in which the brain surface is significantly disrupted may still present a problem.

Surgical Navigation Systems (SNS) have already proven to be a beneficial addition to neurosurgery. The aid that SNS provide in localizing pathologic tissue is invaluable. However, due to brain deformation, SNS use is limited to guidance before the brain has shifted or providing limited information after the shift. Overall, this work shows that game theory can be used as an image processing tool to infer information about physical processes (brain deformation/camera calibration). Incorporating this system into current SNS guidance systems will provide more accurate surgical guidance for many procedures, leading to better detection of pathologic tissue and decreased surgical complications.

Acknowledgments

The authors would like to thank Dustin Scheinost for his work in performing the repeatability experiments associated with the validation of manually-selected fiducial locations. This work was supported in part by the NIH/NIBIB under grant R01EB000473 (Duncan, J.S. P.I.) and the NIH/NLM under grant 5T15LM007056 (Miller, P.L. P.I.).

Appendix A

Derivation of the Displacement Field Optimization

In this appendix, Bayesian analysis is used to develop the four terms of equation (10). The result is a complete cost function used to estimate surface displacement.

1) Intensity Term

The intensity matching is performed on backprojected surfaces. A backprojected surface is defined as $B_i^S = I_i \left(P \left(\widehat{A}_i, x \right) \right) \forall x \in S$ [53]. (See right side of Figure 6.) Here, S is the deformed surface, $S^U + \underline{\mathbf{U}}_{\text{dense}}$, P is the projection function from the surface to the images (as defined in Section II-D) and i represents the camera number (0 or 1).

The intensity term ensures that intensities backprojected from camera 0 onto the deformed surface match the intensities backprojected from camera 1 to that surface and it is written as:

$$\begin{aligned} p \left(\underline{\mathbf{I}}, S^U, \underline{\mathbf{A}} | \underline{\mathbf{U}}_{\text{dense}} \right) &= p \left(I_0, \widehat{A}_0, S^U, I_1, \widehat{A}_1 | \underline{\mathbf{U}}_{\text{dense}} \right) \\ &= p \left(I_0 \left(P \left(\widehat{A}_0, \left(S^U + \underline{\mathbf{U}}_{\text{dense}} \right) \right) \right), I_1 \left(P \left(\widehat{A}_1, \left(S^U + \underline{\mathbf{U}}_{\text{dense}} \right) \right) \right) \right) \quad (13) \\ &= p \left(B_0^S, B_1^S \right) \end{aligned}$$

This formulation emphasizes that there is a single projection function, P , that projects 3D points from the cortical surface into stereo camera space.

The use of normalized cross correlation (NCC) as a match metric follows naturally from this formulation. Assuming the noise in each backprojected image, Ψ_i is additive, Gaussian distributed and independent with zero mean; i.e., $\Psi_i = \widetilde{\Psi}_i + n_i$ where Ψ_i , $i = 0, 1$, the perceived backprojection, is the true projection, $\widetilde{\Psi}$ plus zero mean Gaussian noise, n_i , $i = 0, 1$, it follows that $\Psi_0 = \widetilde{\Psi}_0 + n_0$, $\Psi_1 = \widetilde{\Psi}_1 + n_1 \Rightarrow \Psi_0 = \Psi_1 + n_t$ where $n_t = n_0 + n_1$ and is therefore also Gaussian distributed, leading to:

$$p(\Psi_0, \Psi_1) = \frac{1}{(\sigma \sqrt{2\pi})^n} e^{-\frac{\sum(\Psi_0 - \Psi_1)^2}{2\sigma^2}} \quad (14)$$

where σ is the standard deviation of the backprojected image intensities and n is the number of surface elements in the image overlap region, in which the sum is also taken.

Taking the log of both sides of equation (14) yields:

$$\begin{aligned} \log [p(\Psi_0, \Psi_1)] &= \log \left[\frac{1}{(\sigma \sqrt{2\pi})^n} \right] - \frac{\sum(\Psi_0 - \Psi_1)^2}{2\sigma^2} \\ &= \log \left[\frac{1}{(\sigma \sqrt{2\pi})^n} \right] - \frac{\sum(\Psi_0^2 - 2(\Psi_0)(\Psi_1) + \Psi_1^2)}{2\sigma^2} \quad (15) \end{aligned}$$

This model only accounts for additive noise in each backprojected image. However, if the aperture of each camera is set differently, there may not be an identity transformation between the two images. Using the original variables, in this case, B_0^S may equal $gB_1^S + n_t$, where g is a constant gain factor. This indicates that one image is brighter than the other. To account for this possible affine transformation, the backprojections can be normalized by

subtracting out the mean intensity, $B_i^S - \bar{B}_i^S$. Substituting $\Psi_i = B_i^S - \bar{B}_i^S$ back into equation (15) yields:

$$\log [p(B_0^S, B_1^S)] = \log \left[\frac{1}{(\sigma\sqrt{2\pi})^n} \right] - \frac{\sum \left[(B_0^S - \bar{B}_0^S)^2 - 2(B_0^S - \bar{B}_0^S)(B_1^S - \bar{B}_1^S) + (B_1^S - \bar{B}_1^S)^2 \right]}{2\sigma^2} \quad (16)$$

Since the image intensities in the scene will not change substantially throughout the entire surgery, for all \underline{U}_{dense} , the square of the normalized images, $(B_i^S - \bar{B}_i^S)^2$, should be essentially constant. This is the same as saying that a single camera's intensity histogram will not vary throughout the surgical procedure. In addition, it is assumed that the area of overlap between the two backprojected images will remain fairly constant.

Using the above assumptions and neglecting all the constant terms in equations (14) - (16) yields the probability between the two backprojected images:

$$\log [p(B_0^S, B_1^S)] \propto \frac{\sum (B_0^S - \bar{B}_0^S)(B_1^S - \bar{B}_1^S)}{\sqrt{\sum (B_0^S - \bar{B}_0^S)^2} \sqrt{\sum (B_1^S - \bar{B}_1^S)^2}} \quad (17)$$

In equation (17), the divisor, $\sqrt{\sum (B_i^S - \bar{B}_i^S)^2}$, is a constant that is used to normalize the output between 0 and 1. The result is the familiar formulation for NCC.

Equations (13) and (17) can be combined to yield the intensity term:

$$T_I(\underline{U}_{dense}, \underline{A}) = \log \left[p(\underline{I}, S^U, \underline{A} | \underline{U}_{dense}) \right] = \eta NCC(B_0^S, B_1^S) \quad (18)$$

where η is a normalizing constant. These constants ensure that all terms have similar orders of magnitude.

2) Prior

Since the deformation is smooth, the second derivative of the deformation field should be small, and the displacement at one point should be similar to its neighboring points. Because of this, the displacement field can be modeled as a Markov Random Field, thus implying that \underline{U}_{dense} is sampled from a Gibbs probability density function. This can be expressed in the prior term as:

$$T_U(\underline{U}_{dense}) = \rho e^{-\int |\underline{U}_{dense}''| dS} \quad (19)$$

where ρ is a normalizing constant and \underline{U}_{dense}'' is the second derivative of the dense displacement field.

3) Constants

The stereo camera images, $\underline{\mathbf{I}}$, the sulci in those images, $\underline{\mathbf{K}}$, the preoperative surface, S^U , and sulci on that surface, $\underline{\mathbf{C}}$, are all constants in this framework because they comprise the information supplied to the algorithm. Additionally, while solving for the dense displacement field, the camera calibration parameters from the previous iteration, $\underline{\hat{\mathbf{A}}}$, are also held fixed. Though all of these variables are given, the probabilities of these variables as expressed in the constant terms of equation (10) may not be fixed. While it may be possible to find exact probabilistic definitions for these terms, the process is non-trivial and not easily validated. The added information supplied by the probability of the given constants could possibly enhance the surface tracking algorithm, however, it is not necessary to solve the model. Because of this, the probabilistic definitions defined above are used to motivate the algorithm development rather than exactly define it. To indicate this, matching terms, which incorporate the goals of the conditional probability terms into an intuitive framework are used. The model can then be reformulated by combining equations (5), (10), (18) and (19) as:

$$\begin{aligned} \hat{\underline{\mathbf{U}}}_{\text{dense}} = \underset{\underline{\mathbf{U}}_{\text{dense}}}{\text{argmax}} \log & \left[M \left(\underline{\mathbf{U}}_{\text{dense}} | \underline{\mathbf{I}}, \underline{\mathbf{K}}, \underline{\mathbf{C}}, S^U, \underline{\hat{\mathbf{A}}} \right) \right] \\ = \underbrace{\eta NCC(B_0^S, B_1^S)}_{\text{Intensity Term}} + \underbrace{\log \left[M \left(\underline{\mathbf{K}}, \underline{\mathbf{C}}, \underline{\hat{\mathbf{A}}} | \underline{\mathbf{U}}_{\text{dense}} \right) \right]}_{\text{Feature Term}} + \underbrace{\rho e^{-\int |\underline{\mathbf{U}}_{\text{dense}}''| dS}}_{\text{Prior Term}} \end{aligned} \quad (20)$$

where M represents a matching procedure, rather than a formal probability.

4) Feature Term

The feature matching term from equation (20), $\log [M(\underline{\mathbf{K}}, \underline{\mathbf{C}}, \underline{\hat{\mathbf{A}}} | \underline{\mathbf{U}}_{\text{dense}})]$, can be simplified by considering the sulci outlined in the two camera images $\underline{\mathbf{K}}_0$ and $\underline{\mathbf{K}}_1$ separately. The matching can then be performed in intraoperative stereo image space. Intuitively, the correct displacement field, when applied to the preoperative sulci, will deform those sulci to the same location they were in when imaged by the stereo cameras. If these deformed sulci are projected to the images, by means of accurate camera calibration parameters, they should be exactly aligned with imaged intraoperative sulci. The matching term, therefore, penalizes displacement fields which do not align the imaged sulci with the projected sulci. (See Figure 11 for a pictorial description.)

The feature matching term can therefore be written as:

$$\begin{aligned} T_F \left(\underline{\mathbf{U}}_{\text{dense}}, \underline{\hat{\mathbf{A}}} \right) = & - \int d \left[K_0, P \left(\underline{\hat{\mathbf{A}}}_0, \left(\underline{\mathbf{C}} + \underline{\mathbf{U}}_{\text{dense}}^C \right) \right) \right] dS \\ & - \int d \left[K_1, P \left(\underline{\hat{\mathbf{A}}}_1, \left(\underline{\mathbf{C}} + \underline{\mathbf{U}}_{\text{dense}}^C \right) \right) \right] dS \end{aligned} \quad (21)$$

where $\underline{\mathbf{U}}_{\text{dense}}^C$ is the dense displacement field restricted to the sulci and d is a mean Euclidean distance metric, defined as $d(W, V) = \frac{1}{N} \sum_{i=1}^N \|w_i - v_i\|$, in which W and V have the components $(w_{x1...N}, w_{y1...N}, w_{z1...N})$ and $(v_{x1...N}, v_{y1...N}, v_{z1...N})$ respectively.

5) Displacement Field Cost Function

The displacement field cost function, $C_1(\underline{\mathbf{U}}_{\text{dense}}, \underline{\hat{\mathbf{A}}})$, is thus:

$$\underbrace{T_U(\mathbf{U}_{\text{dense}})}_{\text{smoothness constraint}} + \alpha \left[\underbrace{T_F(\mathbf{U}_{\text{dense}}, \mathbf{A})}_{\text{feature matching}} + \underbrace{T_I(\mathbf{U}_{\text{dense}}, \mathbf{A})}_{\text{intensity correlation}} \right] \quad (22)$$

Appendix B

Derivation of the Camera Calibration Optimization

The cost function for the camera calibration parameters is developed in the following section. As in Appendix A in which the cost function for the displacement field is developed, intuitive matching metrics are used. Equation (11) can thus be written as:

$$\begin{aligned} \hat{\mathbf{A}} &= \underset{\mathbf{A}}{\operatorname{argmax}} \log \left[M(\mathbf{A}, \mathbf{I}, \mathbf{K}, \mathbf{C}, S^U, \hat{\mathbf{U}}_{\text{dense}}) \right] \\ &= \underbrace{\log \left[M(\mathbf{I}, \mathbf{K}, \mathbf{C}, S^U, \hat{\mathbf{U}}_{\text{dense}} | \mathbf{A}) \right]}_{\text{Calibration Term}} + \underbrace{\log \left[M(\mathbf{A}) \right]}_{\text{Prior Term}} \quad (23) \end{aligned}$$

where M represents the matching procedure described in Appendix A.

6) Calibration Term

The calibration term measures the accuracy with which the camera parameters can transform a 3D point to its correct 2D image location. It is difficult to determine calibration accuracy using the backprojected intensities because of ambiguities in correspondence; i.e., a window of backprojected intensity values from one stereo image may have equal correlation with more than one window of backprojected intensities from the other image. The sulci, however, provide accurate feature information from which correspondence is more reliably calculated. Because of this, the sulci on the 3D surface, \mathbf{C} , can provide all the necessary information from the surface itself, S^U . Additionally, since the imaged sulci are the only features of interest, \mathbf{K} can be used to represent the rest of the image, \mathbf{I} . Thus, the calibration term reduces to $\log [M(\mathbf{K}, \mathbf{C}, \hat{\mathbf{U}}_{\text{dense}} | \mathbf{A})]$.

To further evaluate this term, a stereo reconstruction function that gives the 3D location of corresponding points in the stereo images, Φ , is defined. It can be calculated from the initial camera calibration, \mathbf{A} , by determining the rigid transformation between cameras 0 and 1. If this transformation is represented by a rotation, \mathbf{R}_{01} , and translation, \mathbf{T}_{01} , the 3D reconstruction of a set of corresponding points $m_{0i\dots n}$ in image 0 and $m_{1i\dots n}$ in image 1, can be found through the equation $M_{xi}m_{0i} - M_{yi}\mathbf{R}_{01}^T m_{1i} + M_{zi}(m_{0i} \times \mathbf{R}_{01}^T m_{1i}) = \mathbf{T}_{01}$, where $\mathbf{M}_i = [M_{xi}, M_{yi}, M_{zi}]$ is the reconstructed 3D location of corresponding points m_{0i} and m_{1i} [61].

Using the above equations, reconstruction of each of the outlined sulci in \mathbf{K} can be performed and the mean Euclidean distance between these and the 3D deformed sulci can be found.

$$T_c = \left(\mathbf{U}_{\text{dense}}, \mathbf{A} \right) = \int d \left[\Phi \left(K_0, K_1, \mathbf{A} \right), \left(\mathbf{C} + \mathbf{U}_{\text{dense}}^C \right) \right] dS \quad (24)$$

7) Prior Term

The initial camera calibration is performed by locating fiducial points on the cortical surface (using a 3D locator) and the stereo images and determining the optimized best fit transformation between the two fiducial point sets [61]. (See Section II-D.) The prior on the camera calibration, $T_A(\mathbf{A})$, states that as the camera parameters are updated, the projection of the n fiducial points, $L_{0\dots n}$ onto the stereo camera images should be close to imaged fiducial points in cameras 0 and 1, $m_{0i\dots n}$ and $m_{1i\dots n}$ respectively. Assuming Gaussian-distributed errors in selecting fiducial and image locations, the prior term can be expressed as:

$$T_A(\mathbf{A}) = \sum_{i=1}^n \| P(A_0, Li) - m_{0i} \| + \| P(A_1, Li) - m_{1i} \| \quad (25)$$

8) Camera Calibration Cost Function

The camera calibration cost function, $C_2(\mathbf{U}_{dense}, \mathbf{A})$, is thus:

$$\underbrace{T_A(\mathbf{A})}_{\text{fiducial matching}} + \beta \left[\underbrace{T_C(\mathbf{U}_{dense}, \mathbf{A})}_{\text{reconstructed sulci matching}} \right] \quad (26)$$

References

- [1]. Archip, N.; Fedorov, A.; Lloyd, B.; Chrisochoides, N.; Golby, A.; Black, PM.; Warfield, SK. Integration of patient specific modeling and advanced image processing techniques for image-guided neurosurgery; Medical Imaging 2006: Visualization, Image-Guided Procedures, and Display, Proceedings of the SPIE; San Diego, CA. February 12-14 2006; p. 422-429.
- [2]. Audette MA, Siddiqi K, Ferrie FP, Peters TM. An integrated range-sensing, segmentation and registration framework for the characterization of intra-surgical brain deformations in image-guided surgery. Computer Vision and Image Understanding. Feb; 2003 89(2-3):226–251.
- [3]. Ba ar, T.; Jan Olsder, G. Dynamic Noncooperative Game Theory. 2nd Ed.. Academic Press; New York: 1995.
- [4]. Baker S, Nayar SK. Parametric feature detection. International Journal of Computer Vision. 1998; 27(1):27–50.
- [5]. Bates, LM.; Goerss, SJ.; Robb, RA. A method for quantitative validation of image based correction for intraoperative brain shift; Medical Imaging 2000: Image Display and Visualization, Proceedings of the SPIE; San Diego, CA. February 13-15 2000; p. 58-69.
- [6]. Black PM, Moriarty T, Eben A III, Stieg P, Woodard EJ, Gleason PL, Martin CH, Kikinis R, Schwartz RB, Jolesz FA. Development and implementation of intraoperative Magnetic Resonance Imaging and its neurosurgical applications. Neurosurgery. Oct; 1997 41(4):831–845. [PubMed: 9316044]
- [7]. Blumenthal, T.; Hartov, A.; Lunn, K.; Kennedy, FE.; Roberts, DW.; Paulsen, KD. Quantifying brain shift during neurosurgery using spatially tracked ultrasound; Medical Imaging 2005: Visualization, Image-Guided Procedures, and Display, Proceedings of the SPIE; San Diego, CA. February 13-15 2005; p. 388-399.
- [8]. Bouguet JY. Camera calibration toolbox for MATLAB. http://www.vision.caltech.edu/bouguetj/calib_doc/
- [9]. Bozma HI, Duncan JS. A game-theoretic approach to integration of modules. IEEE Transactions on Pattern Analysis & Machine Intelligence. 1994; 16(11):1074–1086.

- [10]. Cao, A.; Dumpuri, P.; Miga, MI. Tracking cortical surface deformations based on vessel structure using a laser range scanner; International Symposium on Biomedical Imaging (ISBI); Washington, DC, USA. April 6-9 2006; p. 522-525.
- [11]. Chakraborty A, Duncan JS. Game-Theoretic integration for image segmentation. *IEEE Transactions on Pattern Analysis and Machine Intelligence*. Jan; 1999 21(1):12–30.
- [12]. Chen Q, Sun QS, Heng PA, Xia DS. Parametric active contours for object tracking based on matching degree image of object contour points. *Pattern Recognition Letters*. Jan; 2008 29(2): 126–141.
- [13]. Clatz O, Delingette H, Talos IF, Golby AJ, Kikinis R, Jolesz FA, Ayache N, Warfield SK. Robust nonrigid registration to capture brain shift from intraoperative MRI. *IEEE Transactions on Medical Imaging*. Nov; 2005 24(11):1417–1427. [PubMed: 16279079]
- [14]. Colchester ACF, Zhao J, Holton-Tainter KS, Henri CJ, Maitland N, Roberts PTE, Harris CG, Evans RJ. Development and preliminary evaluation of VISLAN, a surgical planning and guidance system using intra-operative video imaging. *Medical Image Analysis*. Mar; 1996 1(1): 73–90. [PubMed: 9873922]
- [15]. Comaniciu D, Ramesh V, Meer P. Kernel-based object tracking. *IEEE Transactions on Pattern Analysis and Machine Intelligence*. May; 2003 25(5):564–577.
- [16]. Darolti, C.; Mertins, A.; Hofmann, UG. *Advanced Concepts for Intelligent Vision Systems (ACIVS)*. Vol. 4678. Delft; the Netherlands: Aug 28-31. 2007 A fast level-set method for accurate tracking of articulated objects with an edge-based binary speed term; p. 828-839.
- [17]. DeLorenzo, C.; Papademetris, X.; Vives, KP.; Spencer, DD.; Duncan, JS. Combined feature/intensity-based brain shift compensation using stereo guidance; International Symposium on Biomedical Imaging (ISBI); Washington, DC, USA. April 6-8 2006; p. 335-338.
- [18]. DeLorenzo, C.; Papademetris, X.; Vives, KP.; Spencer, DD.; Duncan, JS. *Medical Image Computing and Computer-Assisted Intervention (MICCAI)*. Vol. 4792. Brisbane, Australia: Nov 1. 2007 A comprehensive system for intraoperative 3D brain deformation recovery; p. 553-561. October 30
- [19]. DeLorenzo, C.; Papademetris, X.; Vives, KP.; Spencer, DD.; Duncan, JS. A realistic brain phantom for 3D deformation recovery; International Symposium on Biomedical Imaging (ISBI); Washington, DC, USA. April 12-15 2007;
- [20]. DeLorenzo, C.; Papademetris, X.; Wu, K.; Vives, KP.; Spencer, DD.; Duncan, JS. *Medical Image Computing and Computer-Assisted Intervention (MICCAI)*. Vol. 4190. Copenhagen, Denmark: Oct 1-6. 2006 Nonrigid 3D brain registration using intensity/feature information; p. 932-939.
- [21]. Duay, V.; Sinha, TK.; D’Haese, PF.; Miga, MI.; Dawant, BM. Non-rigid registration of serial intra-operative images for automatic brain shift estimation; Workshop on Biomedical Image Registration (WBIR); Philadelphia, PA. June 23-24 2003; p. 61-70.
- [22]. Dumpuri P, Thompson RC, Dawant BM, Cao A, Miga MI. An atlas-based method to compensate for brain shift: Preliminary results. *Medical Image Analysis*. Apr; 2007 11(2):128–145. [PubMed: 17336133]
- [23]. Dumpuri, P.; Thompson, RC.; Sinha, TK.; Miga, MI. Automated brain shift correction using a pre-computed deformation atlas; *Medical Imaging 2006: Visualization, Image-Guided Procedures, and Display*, Proceedings of the SPIE; San Diego, CA. February 12-14 2006; p. 430-437.
- [24]. Ferrant M, Nabavi A, Macq B, Black PM, Jolesz FA, Kikinis R, Warfield SK. Serial registration of intraoperative MR images of the brain. *Medical Image Analysis*. Dec; 2002 6(4):337–359. [PubMed: 12426109]
- [25]. Gobbi, DG.; Comeau, RM.; Peters, TM. *Medical Image Computing and Computer-Assisted Intervention (MICCAI)*. Vol. 1935. Pittsburgh, PA: Oct 11-14. 2000 Ultrasound/MRI overlay with image warping for neurosurgery; p. 106-114.
- [26]. Le Goualher, G.; Collins, DL.; Barillot, C.; Evans, AC. *Medical Image Computing and Computer-Assisted Intervention (MICCAI)*. Vol. 1496. Cambridge, MA: Oct 11-13. 1998 Automatic identification of cortical sulci using a 3D probabilistic atlas; p. 509-518.

- [27]. Grimson WEL, Ettinger GJ, White SJ, Lozano-Pérez T, Wells WM, Kikinis R. An automatic registration method for frameless stereotaxy, image guided surgery, and enhanced reality visualization. *IEEE Transactions on Medical Imaging*. Apr; 1996 15(2):129–140. [PubMed: 18215896]
- [28]. Hastreiter P, Rezk-Salama C, Soza G, Bauer M, Greiner G, Fahlbusch R, Ganslandt O, Nimsky C. Strategies for brain shift evaluation. *Medical Image Analysis*. Dec; 2004 8(4):447–464. [PubMed: 15567708]
- [29]. Heikkilä, J.; Silvén, O. *Computer Vision and Pattern Recognition (CVPR)*. San Juan, Puerto Rico: Jun 17-19. 1997 A four-step camera calibration procedure with implicit image correction; p. 1106-1112.
- [30]. Jacob M, Unser M. Design of steerable filters for feature detection using canny-like criteria. *IEEE Transactions on Pattern Analysis and Machine Intelligence*. Aug; 2004 26(8):1007–1019. [PubMed: 15641731]
- [31]. Jolesz FA. Future perspectives for intraoperative MRI. *Neurosurgery Clinics of North America*. Jan; 2005 16(1):201–213. [PubMed: 15561539]
- [32]. Kemper, CA.; Talos, IF.; Golby, A.; Black, PM.; Kikinis, R.; Grimson, WEL.; Warfield, SK. *Medical Image Computing and Computer-Assisted Intervention (MICCAI)*. Vol. 3217. Saint-Malo; France: Sep 26-29. 2004 An anisotropic material model for image guided neurosurgery; p. 267-275.
- [33]. Kim JS, Hong KS. A new graph cut-based multiple active contour algorithm without initial contours and seed points. *Machine Vision and Applications*. Feb; 2008 19(3):181–193.
- [34]. Letteboer MMJ, Willems PWA, Viergever MA, Niessen WJ. Brain shift estimation in image-guided neurosurgery using 3-D ultrasound. *IEEE Transactions on Biomedical Engineering*. Feb; 2005 52(2):268–276. [PubMed: 15709664]
- [35]. Linguraru, MG.; Ballester, MÁG.; Ayache, N. *Medical Image Computing and Computer-Assisted Intervention (MICCAI)*. Vol. 2879. Montréal, Canada: Nov 15-18. 2003 A multiscale feature detector for morphological analysis of the brain; p. 738-745.
- [36]. Lunn KE, Paulsen KD, Liu F, Kennedy FE, Hartov A, Roberts DW. Data-guided brain deformation modeling: Evaluation of a 3-D adjoint inversion method in porcine studies. *IEEE Transactions on Biomedical Engineering*. Oct; 2006 53(10):1893–1900. [PubMed: 17019852]
- [37]. Lunn KE, Paulsen KD, Lynch DR, Roberts DW, Kennedy FE, Hartov A. Assimilating intraoperative data with brain shift modeling using the adjoint equations. *Medical Image Analysis*. Jun; 2005 9(3):281–293. [PubMed: 15854847]
- [38]. Machacek M, Sauter M, Rösgen T. Two-step calibration of a stereo camera system for measurements in large volumes. *Measurements in Science and Technology*. 2003; 14:1631–1639.
- [39]. Mendelson, E. *Introducing Game Theory and Its Applications*. Chapman & Hall/CRC; Boca Raton: 2004.
- [40]. Miga MI, Sinha TK, Cash DM, Galloway RL, Weil RJ. Cortical surface registration for image-guided neurosurgery using laser-range scanning. *IEEE Transactions on Medical Imaging*. Aug; 2003 22(8):973–985. [PubMed: 12906252]
- [41]. Nakajima S, Atsumi H, Kikinis R, Moriarty TM, Metcalf DC, Jolesz FA, Black PM. Use of cortical surface vessel registration for image-guided neurosurgery. *Neurosurgery*. Jun.1997 40:1201–1210. [PubMed: 9179893]
- [42]. Nimsky C, Ganslandt O, Keller B. v. Fahlbusch R. Intraoperative high-field MRI: anatomical and functional imaging. *Acta Neurochir*. 2006; 98(Suppl):87–95.
- [43]. Papademetris X, DeLorenzo C, Flossmann S, Neff M, Vives KP, Spencer DD, Staib LH, Duncan JS. From medical image computing to computer-aided intervention: development of a research interface for image-guided navigation. *The International Journal of Medical Robotics and Computer Assisted Surgery*. 2009; 5:147–157.
- [44]. Papademetris, X.; Jackowski, M.; Rajeevan, N.; Constable, RT.; Staib, Lawrence H. *BioImage Suite: An integrated medical image analysis suite*, Section of Bioimaging Sciences. Dept. of Diagnostic Radiology, Yale School of Medicine; <http://www.bioimagesuite.org>

- [45]. Paul P, Fleig O, Jannin P. Augmented virtuality based on stereoscopic reconstruction in multimodal image-guided neurosurgery: Methods and performance evaluation. *IEEE Transactions on Medical Imaging*. Nov; 2005 24(11):1500–1511. [PubMed: 16279086]
- [46]. Reinertsen, I.; Descoteaux, M.; Drouin, S.; Siddiqi, K.; Collins, DL. *Medical Image Computing and Computer-Assisted Intervention (MICCAI)*. Vol. 3217. Saint-Malo; France: Sep 26-29. 2004 Vessel driven correction of brain shift; p. 208-216.
- [47]. Rivière D, Mangin JF, Papadopoulos-Orfanos D, Martinez JM, Frouin V, Régis J. Automatic recognition of cortical sulci of the human brain using a congregation of neural networks. *Medical Image Analysis*. Jun; 2002 6(2):77–92. [PubMed: 12044997]
- [48]. Roberts DW, Hartov A, Kennedy FE, Miga MI, Paulsen KD. Intraoperative brain shift and deformation: A quantitative analysis of cortical displacement in 28 cases. *Neurosurgery*. Oct; 1998 43(4):749–758. [PubMed: 9766300]
- [49]. Sinha TK, Dawant BD, Duay V, Cash DM, Weil RJ, Thompson RC, Weaver KD, Miga MI. A method to track cortical surface deformations using a laser range scanner. *IEEE Transactions on Medical Imaging*. Jun; 2005 24(6):767–781. [PubMed: 15959938]
- [50]. Sinha, TK.; Duay, V.; Dawant, BM.; Miga, MI. *Medical Image Computing and Computer-Assisted Intervention (MICCAI)*. Vol. 2879. Montréal, Canada: Nov 15-18. 2003 Cortical shift tracking using a laser range scanner and deformable registration methods; p. 166-174.
- [51]. Sinha TK, Miga MI, Cash DM, Weil RJ. Intraoperative cortical surface characterization using laser range scanning: Preliminary results. *Neurosurgery*. Oct; 2006 59(ONS Suppl 4):ONS368–ONS377. [PubMed: 17041506]
- [52]. Škrinjar, O.; Duncan, JS. Stereo-guided volumetric deformation recovery; International Symposium on Biomedical Imaging (ISBI); Washington, DC, USA. July 7-10 2002; p. 863-866.
- [53]. Škrinjar, O.; Nabavi, A.; Duncan, JS. *Mathematical Methods in Biomedical Image Analysis (MMBIA)*. Kauai, HI: Dec 9-10. 2001 A stereo-guided biomechanical model for volumetric deformation analysis; p. 95-102.
- [54]. Škrinjar O, Nabavi A, Duncan JS. Model-driven brain shift compensation. *Medical Image Analysis*. Dec; 2002 6(4):361–373. [PubMed: 12494947]
- [55]. Soza, G.; Grosso, R.; Nimsky, C.; Greiner, G.; Hastreiter, P. *Medical Image Computing and Computer-Assisted Intervention (MIC-CAI)*. Vol. 3217. Saint-Malo; France: Sep 26-29. 2004 Estimating mechanical brain tissue properties with simulation and registration; p. 276-283.
- [56]. Sun, H.; Farid, H.; Rick, K.; Hartov, A.; Roberts, DW.; Paulsen, Keith D. *Medical Image Computing and Computer-Assisted Intervention (MICCAI)*. Vol. 2878. Montréal, Canada: Nov 15-18. 2003 Estimating cortical surface motion using stereopsis for brain deformation models; p. 794-801.
- [57]. Sun H, Lunn KE, Farid H, Wu Z, Roberts DW, Hartov A, Paulsen KD. Stereopsis-guided brain shift compensation. *IEEE Transactions on Medical Imaging*. 2005; 24(8):1039–1052. [PubMed: 16092335]
- [58]. Sun H, Roberts DW, Farid H, Wu Z, Hartov A, Paulsen KD. Cortical surface tracking using a stereoscopic operating microscope. *Neurosurgery*. Jan; 2005 56(ONS Suppl 1):ONS86–ONS97.
- [59]. Sun, H.; Roberts, DW.; Hartov, A.; Rick, K.; Paulsen, KD. Using cortical vessels for patient registration during image-guided neurosurgery - A phantom study; *Medical Imaging 2003: Visualization, Image-Guided Procedures, and Display, Proceedings of the SPIE*; San Diego, CA. February 16-18 2003; p. 183-191.
- [60]. Tao, X.; Davatzikos, C.; Prince, JL. *Medical Image Computing and Computer-Assisted Intervention (MICCAI)*. Vol. 3750. Palm Springs, CA: Oct 26-29. 2005 Using the fast marching method to extract curves with given global properties; p. 870-877.
- [61]. Trucco, E.; Verri, A. *Introductory Techniques for 3-D Computer Vision*. Prentice-Hall, Inc.; Upper Saddle River, New Jersey: 1998.
- [62]. Tu Z, Zheng S, Yuille A. Shape matching and registration by data-driven EM. *Computer Vision and Image Understanding*. Mar; 2008 109(3):290–304.
- [63]. Tu Z, Zheng S, Yuille AL, Reiss AL, Dutton RA, Lee AD, Galaburda AM, Dinov I, Thompson PM, Toga AW. Automated extraction of the cortical sulci based on a supervised learning

- approach. *IEEE Transactions on Medical Imaging*. Apr; 2007 26(4):541–552. [PubMed: 17427741]
- [64]. Warfield SK, Talos F, Tei A, Bharatha A, Nabavi A, Ferrant M, Black PM, Jolesz FA, Kikinis R. Real-time registration of volumetric brain MRI by biomechanical simulation of deformation during image guided neurosurgery. *Computing and Visualization in Science*. Jul; 2002 5(1):3–11.
- [65]. Wittek, A.; Kikinis, R.; Warfield, SK.; Miller, K. *Medical Image Computing and Computer-Assisted Intervention (MICCAI)*. Vol. 3750. Palm Springs, CA: Oct 26-29. 2005 Brain shift computation using a fully nonlinear biomechanical model; p. 583-590.
- [66]. Zhou Y, Thompson PM, Toga AW. Extracting and representing the cortical sulci. *IEEE Computer Graphics and Applications*. May-Jun;1999 19(3):49–55. [PubMed: 20830215]

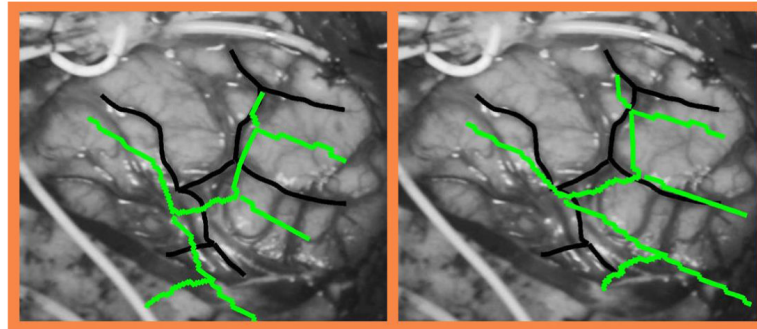


Fig. 1. Intraoperative image indicating the misalignment of the projected sulci (green) with the intraoperative imaged sulci positions (black), due to either camera calibration errors (left) or cortical surface deformation (right).

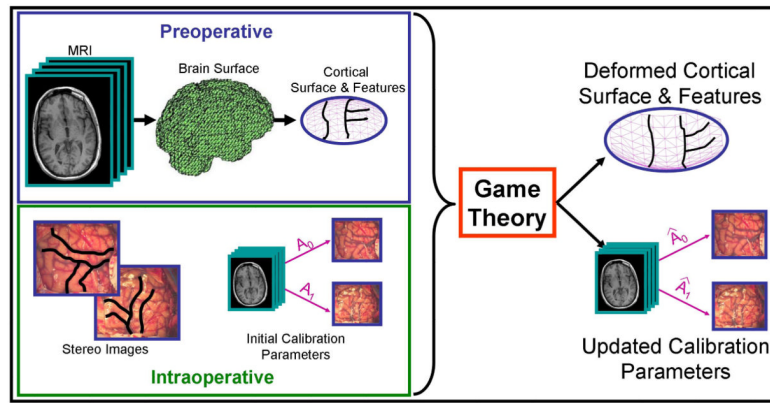


Fig. 2. The game theoretic algorithm uses intraoperative information to guide the estimation of cortical surface deformation and update camera calibration parameters. This algorithm was developed using a Bayesian approach.

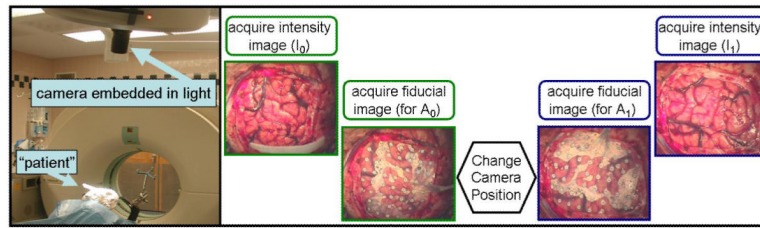


Fig. 3.
Left: A view of the surgical camera embedded in the OR light fixture during a phantom experiment. The overall setup is the same for surgical applications. **Right:** The method of acquiring fiducial points in the OR and an example of typically-acquired images.

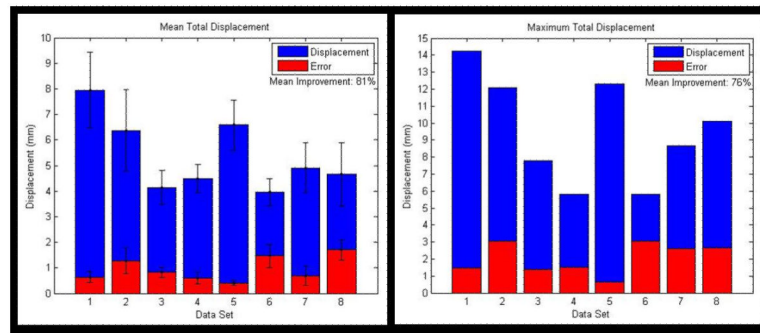


Fig. 4. Mean and maximum displacement (blue) with mean and maximum residual error (red) for eight intraoperative neocortical epilepsy data sets. The algorithm was implemented with $\alpha = 4$, $\beta = 0.83$, $\nu = 0.1$, and $\eta = 25$ for all cases. (See Appendices A and B for algorithm equations.)

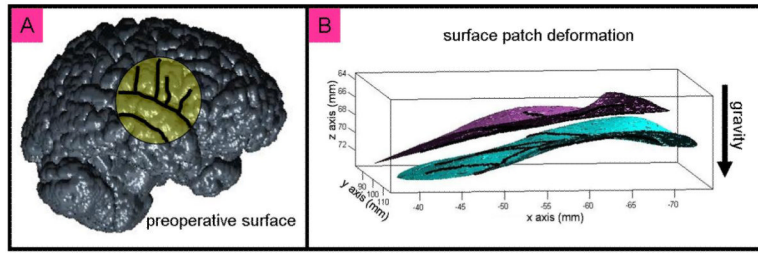


Fig. 5.

A: Preoperative Surface of Data Sets 4 and 5, Acquired from MRI. The region that deforms during surgery is highlighted in yellow and features used to aid the algorithm are shown in black. **B:** Cortical Surface Deformation Results at Two Time Points. The purple and blue surfaces represent the algorithm tracking results for data sets 4 (2 hours into surgery) and 5 (3.25 hours into surgery), respectively. The distance between the two surfaces shows the cortical shift in that time, as calculated by the game theoretic algorithm. Sulci used as features are again highlighted in black. The surfaces mainly deformed in the direction of gravity, as indicated by the arrow.

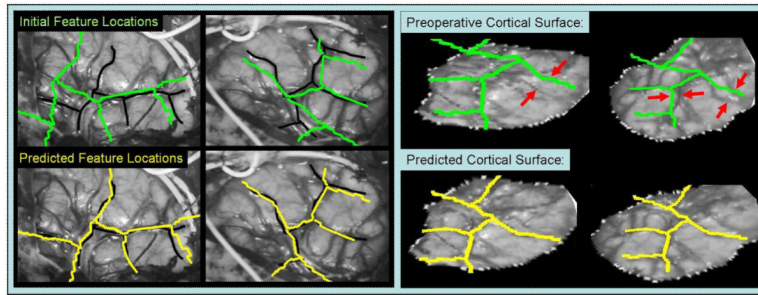


Fig. 6.

Data Set #4, Two Hours into Surgery. **Left:** Intraoperative Stereo Images of the Cortical Surface. The projected predicted features (yellow) are better aligned with the features outlined from the intraoperative images (black) than the projected preoperative features (green). **Right:** Intraoperative Cortical Surface with Backprojected Intensities. Backprojection is achieved by using the calibration parameters to project each element of the surface to one of the stereo images and assigning the corresponding image intensities to the surface elements. (See Appendix A.) The stereo images were manually cropped to include only brain surface intensities. Therefore, each of the surface elements was either assigned one of these image intensities or appears black, meaning no intensity was assigned. The predicted cortical surface reduces the mismatch, shown by the red arrows, between the backprojected sulci and the sulci lying on the surface (green/yellow).

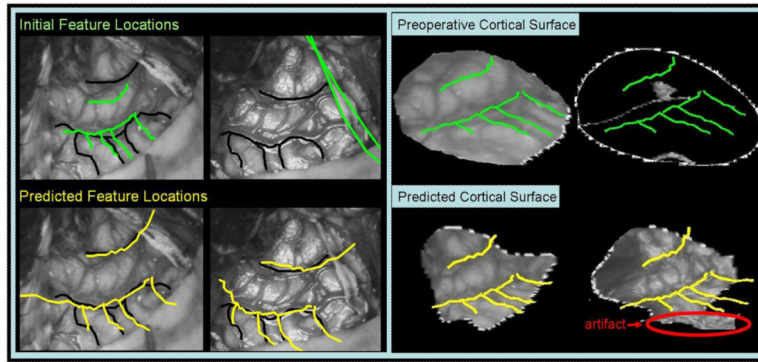


Fig. 7. Data Set #5, 3.25 Hours into Surgery **Left:** Intraoperative Stereo Images of the Cortical Surface. The initial calibration of the camera 1 (right) is so inaccurate, that the features (green) do not project to the image field of view. The algorithm is able to correct this error and predict the cortical surface to within 1 mm. **Right:** Intraoperative Cortical Surface with Backprojected Intensities. Most of the right stereo image backprojected intensities do not fall on the preoperative surface due to calibration inaccuracies and the surface position. With the updated calibration and deformation parameters, intensities and features from both images are better aligned, though there is still some distortion outside the calibration region.

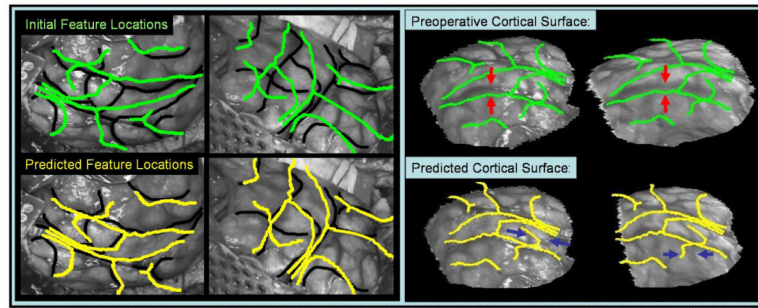


Fig. 8.

Data Set #8 **Left:** Intraoperative Stereo Images of the Cortical Surface. Preoperative sulci projected with initial calibration parameters are shown in green. The algorithm is able to correct some mismatch between these and the imaged sulcal locations (black). The residual misalignment of predicted projected features (yellow) is most likely due to the poor positioning of the electrode grid. **Right:** Intraoperative Cortical Surface with Backprojected Intensities. Overall, the game theoretic result for data set #8 decreased the tracking error and improved the deformation estimation. Evidence of this can be seen in the reduction of feature-matching error shown by the red arrows. However, some feature mismatch (blue arrows) is still evident in the backprojected images from the algorithm-predicted surfaces.

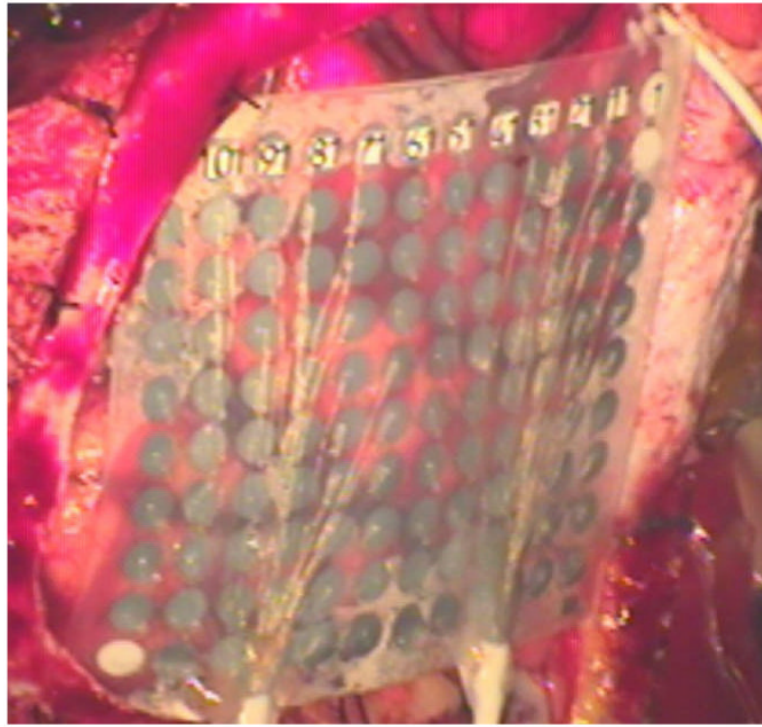


Fig. 9. Electrode Grid Used for Calibration of Data Set #8. The shape of the brain and the size of the dural opening prevented the grid from lying flat on the brain surface.

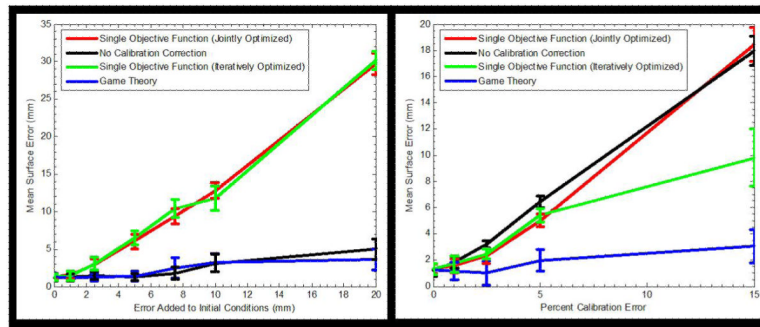


Fig. 10. Algorithm Robustness Comparison. **Left:** Sensitivity to Initial Surface Position. **Right:** Sensitivity to Initial Camera Calibration Errors.

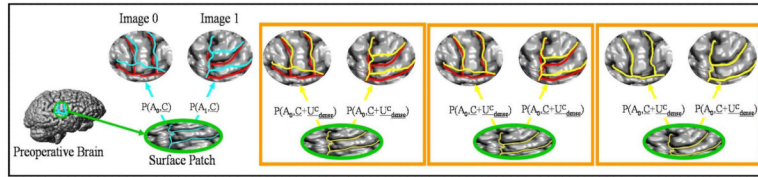


Fig. 11.

Pictorial Description of the Feature Term. The far left image shows the brain surface as extracted from the preoperative MRI and the region of that surface (surface patch) that deforms during surgery. Using a projection function, 3D sulci from the surface patch are projected onto the 2D stereo camera images. Assuming an accurate camera calibration, the mismatch between the projected features (cyan) and the imaged features (red) is due to surface deformation. The right orange boxes show the effects of various displacement fields applied to the surface patch. The distance between the projected sulci from those patches (yellow) and the imaged sulci (red) is measured for each applied displacement. In this case, the displacement field applied to the patch on the far right is the most likely because it best aligns the two sets of features.

TABLE I

PATIENT INFORMATION. ALL PATIENTS UNDERWENT EITHER ELECTRODE IMPLANTATION OR TISSUE RESECTION FOR NEOCORTICAL EPILEPSY. ALL STEREO IMAGES WERE ACQUIRED POST ARACHNOID OPENING AT THE TIME INTO SURGERY INDICATED BY THE LAST COLUMN

Case #	Patient #	Age	Sex	Reason for Surgery	Time (mins)
1	1	40	F	left temporal resection for epilepsy	95
2	2	38	M	electrode insertion (left hemisphere) for epilepsy monitoring	230
3	2	38	M	electrode insertion (right hemisphere) for epilepsy monitoring	230
4	3	55	M	right temporal resection for cavernous malformation	120
5	3	55	M	right temporal resection for cavernous malformation	195
6	4	18	F	insertion of electrodes for epilepsy monitoring	200
7	5	38	M	insertion of electrodes for epilepsy monitoring	180
8	5	38	M	insertion of electrodes for epilepsy monitoring	225

TABLE II

CAMERA CALIBRATION ERROR QUANTIFICATION. THIS TABLE SHOWS THE PERCENT CHANGE OF EACH CALIBRATION PARAMETER FROM ITS INITIALIZED VALUE AS CALCULATED BY GAME THEORETIC ALGORITHM. THE INITIAL CALIBRATION OF CAMERA POSITION 1 WAS INACCURATE, AS EVIDENCED BY FIGURE 7 AND AS SHOWN BY THE CALCULATED PERCENT CHANGE NEEDED TO CORRECT THE PARAMETERS

camera position	focal length	rotation angle	translation	principle point	distortion coeff.
0	2.4%	2.8%	6.6%	13.9%	90.3%
1	70.1%	7.1%	11.8%	48.6%	67.7%